RESEARCH ARTICLE

ESPL WILEY

Characterization of landslide displacements in an active fault zone in Northwest China

Xuguo Shi[1]　|　Xie Hu[2]

[1]School of Geography and Information Engineering, China University of Geosciences, Wuhan, China

[2]College of Urban and Environmental Sciences, Peking University, Beijing, China

Correspondence
Xie Hu, College of Urban and Environmental Sciences, Peking University, Beijing, China.
Email: hu.xie@pku.edu.cn

Abstract

Landslides can be caused by natural forcing and anthropogenic activities. Zhouqu County (China) on the eastern margin of Qinghai-Tibet Plateau is set within the active Pingding-Huama fault zone with evident fractures on the land surface. Frequent landslides and debris flows have occurred in this region due to river erosion, rainfall and deforestation. Here we quantified the slope movements using time-series synthetic aperture radar interferometry (InSAR) based on the ascending and descending Sentinel-1 satellite images acquired between October 2014 and August 2020. We observed distinct displacements in the highly fractured fault zone. The eastward and vertical displacement time series between February 2017 and July 2020 were constrained by the common-day ascending and descending acquisitions. The eastward rates (461 mm/year) were greater than those in the vertical direction (−185 mm/year). We also note displacement discontinuities across the thrust faults beneath the Suoertou and Zhongpai landslides. Seasonal variations in the displacement time series suggest that the cyclic rainfall is the primary driver for the mass wasting processes rather than the tectonic loading. As a complement to *in situ* observations, our results demonstrate that InSAR is an effective tool to characterize the spatio-temporal nature of landslide displacements in complicated geological environments.

Plain Language Summary: Zhouqu County in the Pingding-Huama fault zone in the eastern margin of Qinghai-Tibet Plateau is identified as a high priority site to research on clusters of landslides and debris flows in a mixed geodynamic setting of active tectonics, seasonal rainfall, river erosion and anthropogenic activities. However, our knowledge about landslide kinematics in this complicated region is still limited. We relied on remote sensing images from one ascending and one descending Sentinel-1 satellite tracks to constrain the spatial–temporal displacement dynamics of active landslides from 2014 to 2020. The spatial patterns of displacements are determined by thrust faulting, river erosion, and anthropogenic activities. The temporal variations of landslide speed are mainly controlled by the seasonal rainfall rather than the tectonic loading.

KEYWORDS
displacements, InSAR, Pingding-Huama fault, rainfall-driven landslides, slow-moving landslides

1 | INTRODUCTION

Landslides generalize the mass wasting behaviors downhill and are identified as one of the major destructive natural hazards in mountainous regions. From 2004 to 2016, 4 862 non-earthquake-induced catastrophic landslides in the world killed 55 997 people. About 75% of the events occurred in Asia, especially in the southern margins of the Himalayas (Froude & Petley, 2018). Natural driving

forces such as intensive rainfall, land degradation, wind and river erosion and earth shaking (e.g., earthquakes, volcanoes and quarry blasts) can mobilize slopes or even lead to catastrophic failures (Bontemps et al., 2020; Cheaib et al., 2022; Chen et al., 2014; Fan et al., 2019, 2021; Lacroix et al., 2014; Lacroix, Dehecq, & Taipe, 2020). Landslide damage to life and property has continued to increase throughout the past century (Froude & Petley, 2018; Huang & Li, 2011).

In the context of active tectonics, river erosion and rainfall, as well as anthropogenic deforestation and constructions (Ma et al., 2021; Ren, 2014; Shu & Yang, 2012), Zhouqu County in the Pingding-Huama fault zone is vulnerable to landslides and debris flows. Frequent slope failures of the Jiangdingya landslide (Figure 1) occurred in 1807, 1985, 1988, 1990, 1991 and 2018 (Guo

et al., 2019), which dammed the Bailong River and destroyed the infrastructures multiple times. More than 11 debris flows occurred in Sanyanyu since 1823 (Hu, Ge, & Cui, 2010) (Figure 1). The debris flows in Sanyanyu and Luojiayu on 8 August 2010 claimed 1 765 lives and destroyed more than 5 500 households (Tang et al., 2011; Yu et al., 2015). The rainfall drove the reactivation of the Yahuokou landslide in July 2019, which swept a distance of 500 m downslope with a volume of 3.92×10^6 m^3, destroyed several buildings and dammed the Min River (Dou & Zhang, 2021). The Xieliupo and Suoertou landslides have been creeping for several years (Jiang et al., 2016; Sun et al., 2015; Zhang et al., 2018), putting hundreds of lives at risk. Therefore, Zhouqu County can be considered as a high priority site to investigate the landslide behaviors in the complexity of faults and watercourses.
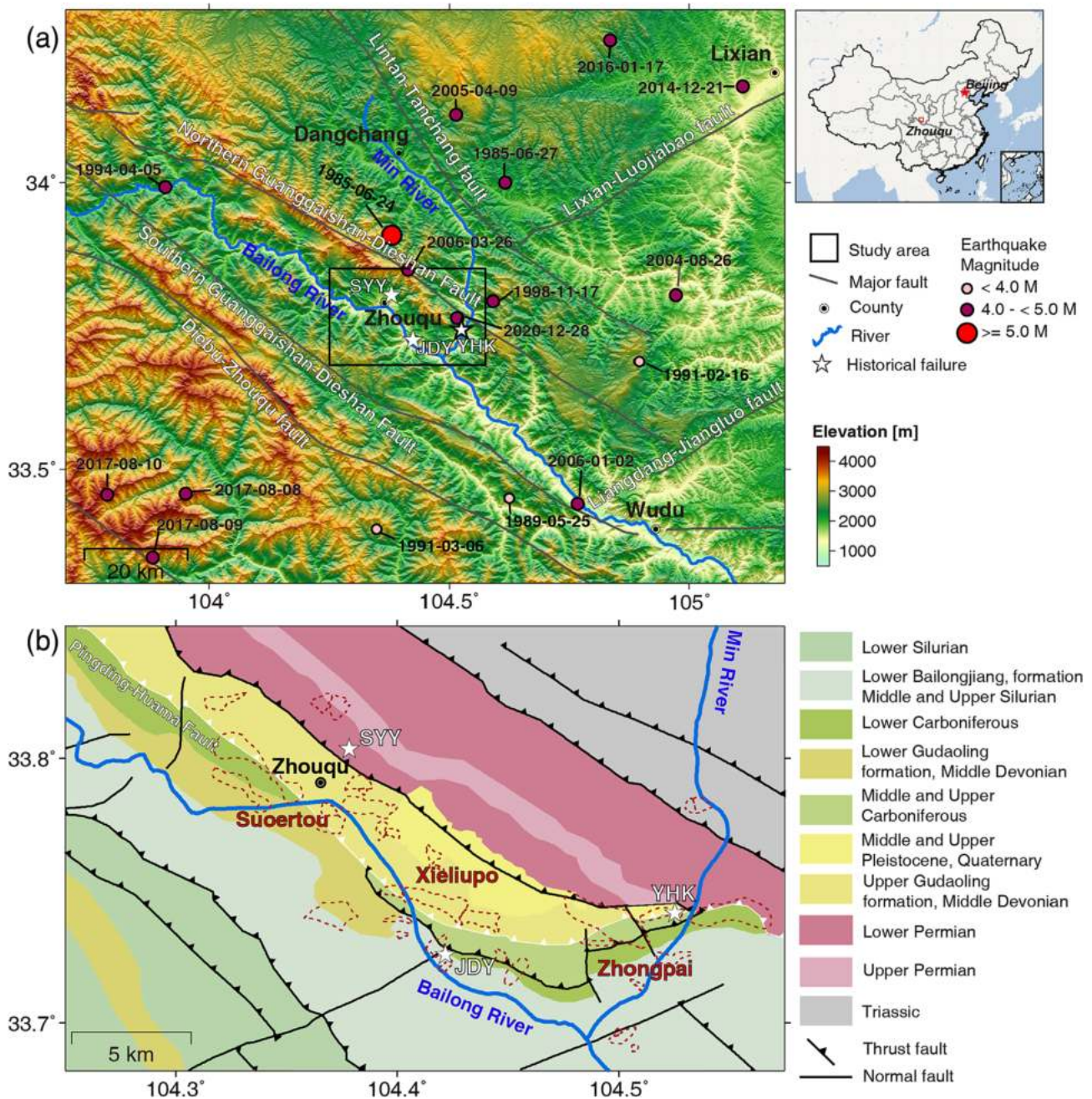

FIGURE 1 (a) Topography and (b) geological map of the Zhouqu County (modified from Schäbitz et al., 2018; Yu et al., 2015). The red dashed polygons in plane b outline the landslides mapped from InSAR results in this study. The SYY, JDY and YHK represent locations of Sanyanyu debris flow, Jiangdingya and Yahuokou landslides occurred on 7 August 2010, 12 July 2018 and 16 July 2019, respectively. [Color figure can be viewed at wileyonlinelibrary.com]

Traditional displacement monitoring tools, for example, piles, inclinometers, extensometers, crack gauges and Global Navigation Satellite System (GNSS)/Global Positioning System (GPS), have been installed on selected landslides in Zhouqu (Hou et al., 2020; Jiang et al., 2016; Meng et al., 2013). With an advantage of hundreds of kilometers' swath width, Synthetic Aperture Radar (SAR) satellite images were added to measure the ground displacements in landslide-prone regions (e.g., Shi et al., 2022). The interferometric SAR (InSAR) method, relying on the phase recorded in the backscattering electromagnetic waves, enables us to measure ground displacements along the line-of-sight (LOS, a.k.a., range) direction (Hanssen, 2001; Lu & Dzurisin, 2014). The accuracies of InSAR method are primarily limited by atmospheric signals and digital elevation model (DEM) errors and intrinsic geometric distortion in mountainous region (Shi et al., 2019b). Time series InSAR methods, for example, persistent scatterer InSAR (PSI) (Ferretti, Prati, & Rocca, 2001) and small baselines subset (SBAS) InSAR (Berardino et al., 2002), can achieve high-accuracy ground displacement measurements based on coherent scatterers in a stack of interferograms. PSI utilizes a series of interferograms referring to a single reference image and focuses on persistent scatterers (e.g., buildings and bare rocks), which usually remain coherent during time. SBAS InSAR relies on interferograms generated by images with short temporal and spatial baselines to minimize decorrelation and focuses on both persistent and slowly decorrelated scatterers. SBAS InSAR usually has a better performance in monitoring displacements in natural environments such as landslides.

Multi-source, multi-band and multi-temporal SAR satellite datasets, for example, X-band COSMO-SkyMed data during 2010–2012 (Wasowski & Bovenga, 2014), C-band ENVISAT Advanced Synthetic Aperture Radar (ASAR) data during 2003–2010 (Zhang et al., 2016) and Sentinel-1 descending data during 2017–2018 (Dai et al., 2021; Li et al., 2023), and L-band ALOS PALSAR ascending data during 2007–2010 (Sun et al., 2015; Zhang et al., 2018), have been used to identify active slopes in Zhouqu using time-series InSAR methods such as PSI, SBAS InSAR, and temporarily coherent point (Zhang et al., 2012a) InSAR. Sentinel-1 is superior to ALOS-1 PALSAR-1 and Envisat ASAR datasets in terms of a shorter revisit time (Dai et al., 2021). Sun et al. (2016) applied the multi-temporal InSAR analysis using the ascending and descending Envisat ASAR datasets and one ascending ALOS-1 PALSAR-1 dataset during 2008–2010 as well as the surface–parallel slip assumption to constrain the three-dimensional displacements of Xiuliupo landslide. We note that previous landslide displacement mapping using multi-temporal InSAR datasets mostly focused on one-dimensional line-of-sight or slope-parallel displacement measurements, which limit our ability to interpret the results. The complete 3D displacements offer more details on ground surface dynamics (Hu et al., 2014). The shorter revisit time of Sentinel-1 mission allows us to better compare the displacement time series with rainfall. Beyond that, a joint analysis of ascending and descending Sentinel-1 datasets provides distinct imaging perspectives to unveil landslide displacement details.

In our study, we mapped the slope displacements in Zhouqu based on time-series InSAR method using Sentinel-1 datasets from October 2014 to August 2020. Two-dimensional displacement time series were constrained by compiling the common-day ascending and descending acquisitions from February 2017 to July 2020. The horizontal east–west displacements were three to four times of the vertical displacements. The high-frequency signals in the displacement field coincided with the tectonic faults. Displacement time series suggested a temporal correlation with seasonal rainfalls.

2 | THE STUDY AREA

Zhouqu County is in the eastern margin of the Tibetan Plateau, where the western wing of the West Qinling Mountains sits beside the Min Mountains. This tectonic zone is featured with rugged mountains and deeply incised valleys (Yu et al., 2015). The altitude of the inclined land surfaces to the southeast ranges between 4 500 and 1 000 m above the sea level (Figure 1a). The black circles in Figure 1a represent the historic earthquakes with magnitudes larger than 2.0 since 1900 from the United States Geological Survey (https://earthquake.usgs.gov).

The lithology of our study area mainly contains the Silurian slates and phyllites, Permian limestones, Devonian limestones and slates, Carboniferous limestones and Triassic sandstone, slates and phyllites (Wang, 2013). The phyllites and limestones are characterized by highly weakened and water-bearing materials, which are subject to erosion and weathering. Quaternary loess is generally distributed in the ridges, terraces and alluvial fans of Bailong River and other secondary streams (Yu et al., 2015). It is an accumulation of aeolian denudation and erosion with a thickness less than 40 m. The loess ridges and terraces were later reclaimed and cultivated (Shu & Yang, 2012).

The Bailong River basin encompasses multiple strands of active strike-slip and thrust faults (Kirby et al., 2003) (Figure 1). Various fault strands in different dimensions affect the formation and development of slow-moving landslides and slope failures. The Pingding-Huama fault is a primary one in the Guanggaishan-Dieshan fault zone (Yang et al., 2013; Yu et al., 2012), which can be divided into the eastern and western segments by Min River in Dangchang County (Figure 1). The reverse slip rates in the western segments are 0.49 ± 0.08 to 1.15 ± 0.28 mm/year and the left-lateral strike-slip rates are 0.51 ± 0.13 mm/year (Yu et al., 2012). GNSS measurements during 2009–2011 revealed a strike-slip rate of 1.4 mm/year and a thrust rate of 3.7 mm/year, respectively (Chen et al., 2012). The bedrock is deeply fractured and highly weathered (Yu et al., 2015), which provides favorable conditions for landsliding. More than 2 000 landslides occurred in Zhouqu and Wudu Counties (Schäbitz et al., 2018). A total of 878 landslides triggered by the magnitude 8.0 Wenchuan earthquake in 2008 were in Dangchang, Zhouqu, and Wudu Counties (Bai et al., 2012). We detected 34 active landslides (dashed polygons in Figure 1b), including the Suoertou, Xieliupo, and Zhongpai landslides. The Suoertou and Xieliupo landslides have been in motion for more than one century (Jiang et al., 2016; Sun et al., 2015). Table S1 shows the geographic locations, slope, aspect, area, and altitude of these 34 landslides. Yet we lack information about when did these landslides activate/reactivate.

We used a 10-m-resolution land cover map (Brown et al., 2022) generated by Sentinel-2 images acquired on 27 September 2019 (Figure S1). The high mountain areas are covered by trees while the lower and flat areas are covered by grass, shrub and scrub. Anthropogenic disturbances from buildups and farmland are mainly concentrated along the Bailong and Min riverbanks. Zhouqu County has the continental monsoon climate (Zhang et al., 2012b). The local climate is controlled by atmospheric circulation and topography, characterized

by vertical climate zoning and distinct dry and wet seasons. The precipitation from June to September accounts for approximately 75% of the annual precipitation total (Tang et al., 2011). Frequent rainstorms promote undercutting and erosion, which may further instigate landslides and debris flows (Fan, 2006).

3 | GROUND DISPLACEMENT MEASUREMENTS

3.1 | InSAR methodology

We obtained Sentinel-1 images from ascending track (S1-A) and descending track (S1-D) (Table S2 and Figure S2) to map the displacements of active slopes in Zhouqu County. The ascending and descending tracks share the same 96 acquisition dates between February 2017 and July 2020, allowing us to well constrain the 2D displacement time series without bias in time. Images acquired on 27 April 2018 were selected as the reference of co-registration. An enhanced spectral diversity method (Jiang, 2020) using ALOS World 3D-30 m (AW3D30) and Precise Orbit Determination (POD) products was employed to co-register all the secondary images to the reference images. We only considered consecutive images to generate interferometric pairs with short temporal intervals and to reduce the temporal decorrelation and phase unwrapping errors. Multi-looks of 4 by 1 in range and azimuth and a Goldstein filter (Goldstein & Werner, 1998) with a 16×16-pixel window size were applied to enhance the signal to noise ratio.

The phase components of each pixel are given by

$$\varphi = W\{\varphi_{\text{disp}} + \varphi_{\text{atm}} + \varphi_{\text{orb}} + \varphi_{\text{dem}} + \varphi_{\text{n}}\} \quad (1)$$

where φ_{disp}, φ_{atm}, φ_{orb}, φ_{dem} and φ_{n} are the phase components caused by ground displacement, atmospheric phase screen, orbital ramps, DEM error and noise. $W\{\cdot\}$ is the wrapping operation. We selected coherent pixels based on the amplitude dispersion and phase stability indices (Ferretti, Prati, & Rocca, 2001). We discarded pixels with temporal coherence smaller than 0.3 in phase unwrapping. We removed the spatially correlated orbital ramps and the elevation-correlated atmospheric phase screen in the unwrapped interferograms using a quadratic model (Sun et al., 2015).

$$\varphi_{\text{orb}} + \varphi_{\text{atm}} = a_0 + a_1 x + a_2 y + a_3 xy + a_4 x^2 + a_5 y^2 + bh \quad (2)$$

where a_i ($i = 1, 2, ..., 5$) is the orbital phase ramp coefficients, x and y are the rows and columns in the radar coordinates, and b is the linear coefficient to the elevation h. The DEM errors were inverted based on the mathematical relationship between the perpendicular baselines and unwrapped phases (Schmidt & Bürgmann, 2003).

$$\varphi_{\text{dem}} = -\frac{4\pi}{\lambda} \frac{B}{R \sin\theta} \Delta h \quad (3)$$

where B, Δh, λ, R, θ are the perpendicular baseline, DEM error, wavelength, slant range, and incidence angle, respectively. The displacement time series were retrieved using least-squares method from the corrected, unwrapped interferograms.

3.2 | 2D displacement solution

The InSAR-derived displacements are one-dimensional along the LOS direction, which is projected from the complete 3D displacements (Fujiwara et al., 2000; Shi et al., 2021).

$$d_U \cos\theta - d_E \cos\alpha \sin\theta + d_N \sin\alpha \sin\theta = d_{LOS} + \delta_{LOS} \quad (4)$$

where d_U, d_E, d_N are displacements measured in the vertical, east, and north directions, respectively, α and θ are the satellite heading angle and nominal incidence angle and d_{LOS} and δ_{LOS} are the observed LOS displacements and the respective errors.

Generally, the contribution of the north–south component of the surface displacement to the satellite line-of-sight length change is negligible relative to the east–west and the up-down components (Shi et al., 2019b). To co-locate the pixels from the ascending and descending orbits, we selected the descending dataset as the reference, and pixels in the ascending dataset within 20 m of pixels in the descending dataset were selected and averaged. We established two equations with two unknowns d_U, d_E considering Euler rotations.

$$\begin{bmatrix} \cos\theta^{asc} - \cos\alpha^{asc} \sin\theta^{asc} & \cos\theta^{desc} - \cos\alpha^{desc} \sin\theta^{desc} \end{bmatrix} \begin{bmatrix} d_U \\ d_E \end{bmatrix}$$
$$= \begin{bmatrix} d_{LOS}^{asc} \\ d_{LOS}^{desc} \end{bmatrix} + \begin{bmatrix} \delta_{LOS}^{asc} \\ \delta_{LOS}^{desc} \end{bmatrix} \quad (5)$$

where the superscripts *asc* and *desc* indicate measurements from ascending and descending datasets, respectively. A weighting matrix W was determined by the standard deviation σ of measurements.

$$W = \begin{bmatrix} \dfrac{1}{(\sigma_{asc})^2} & 0 \\ 0 & \dfrac{1}{(\sigma_{desc})^2} \end{bmatrix} \quad (6)$$

The final 2D displacements were solved by the least-squares method using the LOS displacements from ascending and descending datasets. We also extracted 2D displacement time series using images acquired on the same dates based on Equation (4).

4 | RESULTS

4.1 | The 2D displacements

LOS displacements are one-dimensional slant range measurements with respect to the position of the satellite sensor. Figure 2 shows the LOS displacement rates from S1-A and S1-D between October 2014 and August 2020. The positive or negative values represent ground movements towards or away from the satellite sensor, respectively. The S1-A and S1-D trajectories view the ground targets at distinct directions, and their measurements were opposite in sign, as illustrated in our results of the Suoertou, Daxiaowan and Zhongpai landslides. The maximum displacement rates reached >280 mm/year moving away from the ascending satellite sensor and >250 mm/year towards the descending satellite sensor. The outstanding deforming areas from both orbits were consistent. We detected 34 active
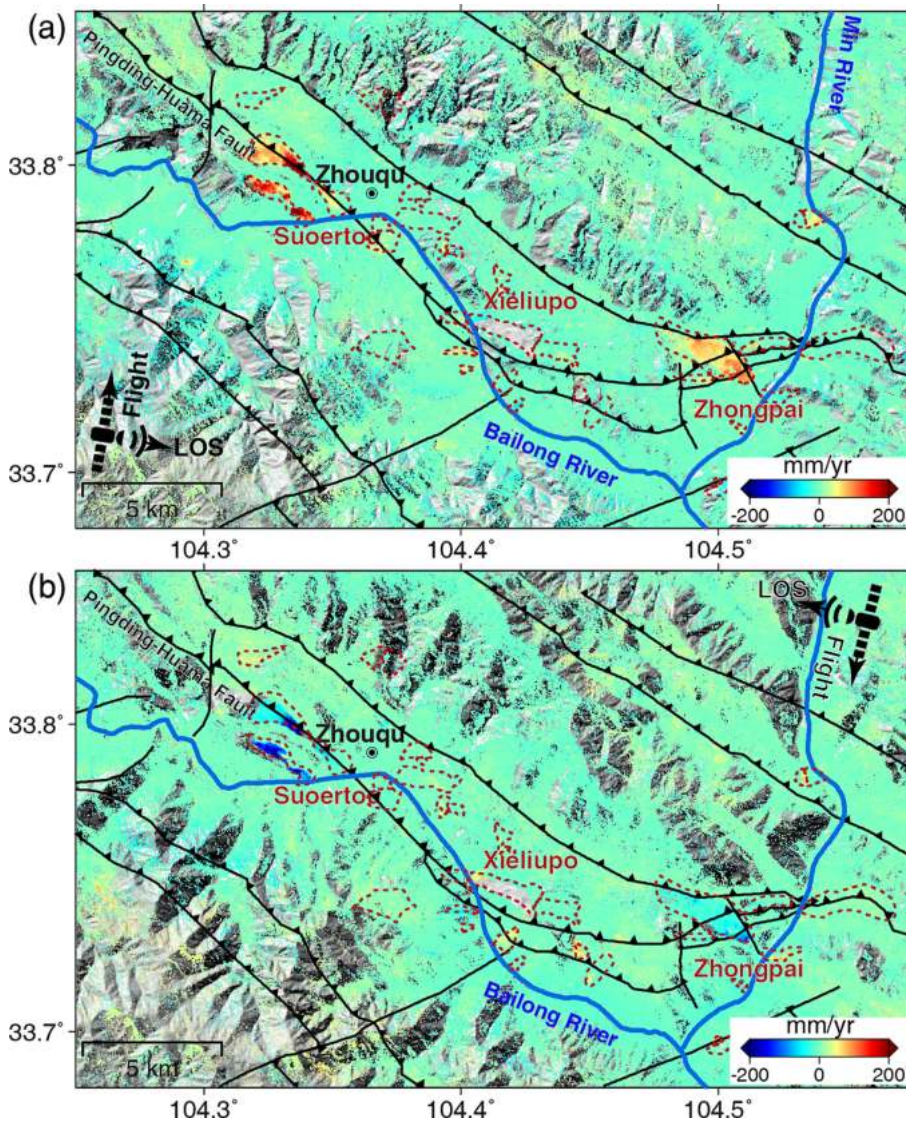
FIGURE 2 Displacement rates of Zhouqu County in the line-of-sight (LOS) direction of (a) S1-A and (b) S1-D. [Color figure can be viewed at wileyonlinelibrary.com]

landslides in areas of 0.4–3.7 km^2 and the total area is ∼23.6 km^2 (Table S1). All landslides are distributed within 1.5 km to the faults in the vicinity of the Bailong River. The rocks in fault zone and the surrounding areas are mostly compressed and broken with joints and fissures on both sides of the fault zone (Qi et al., 2021).

We generated 2D displacement maps from measurements along the S1-A and S1-D LOS (Figure 3). Positive values in Figure 3a,b suggest horizontally eastward and vertically upward movements. The horizontal rates range from −126 to 461 mm/year while the vertical rates range from −185 to 160 mm/year. The upward displacements might be caused by compression and accumulation of materials at the foot of landslides. Vertical displacement rates vary significantly within landslides due to smaller signal-to-noise ratio and irregular basal surfaces (Li et al., 2021). The horizontal east–west displacements are generally consistent with the slope aspects (Figure S3).

4.2 | Suoertou and Daxiaowan landslide displacements

The Suoertou and Daxiaowan landslides are two giant landslides ∼3 km west of Zhouqu. The bedrocks and soil matrix of these two landslides are extremely fragmented (Dai et al., 2021; Jiang

et al., 2015; Qi et al., 2021). The displacement rates in the LOS, eastward, and vertical directions of these two landslides are shown in Figure 4.

The reactivated Suoertou landslide is approximately 4 200 m in length with an elevation difference of 900 m (Jiang et al., 2015). The moving direction of Suoertou landslide is S135°E with an average slope of 12°. The thickness varies from 20 to 100 m with a volume of >8.8 × 10^7 m^3 (Huang et al., 2013b). The Suoertou landslide has been creeping at rates of 300–600 mm/year since 1970s (Jiang & Wen, 2014). The monitoring pile demonstrates that the cumulative displacements were 3–8 m during 1991–1999 and 0.4–1.1 m during 2008–2010 (Huang et al., 2013b). The Suoertou landslide has distinct sections in terms of the composition, morphological and hydrological environments (Figure 4). The displacements in the middle section were larger than that in the upper and lower sections. The rates in the middle section of the Suoertou landslide were −256 and 271 mm/year in the LOS direction from S1-A and S1-D, respectively. To cross-validate the results from ascending and descending orbits, we projected the LOS displacement time series to the downslope direction defined by the slope aspect (Hu et al., 2018b) at P1 located in the middle section and P2 located in the lower section (Figure 5a,c). The averaged downslope displacement difference between the common-day measurements from ascending and descending datasets
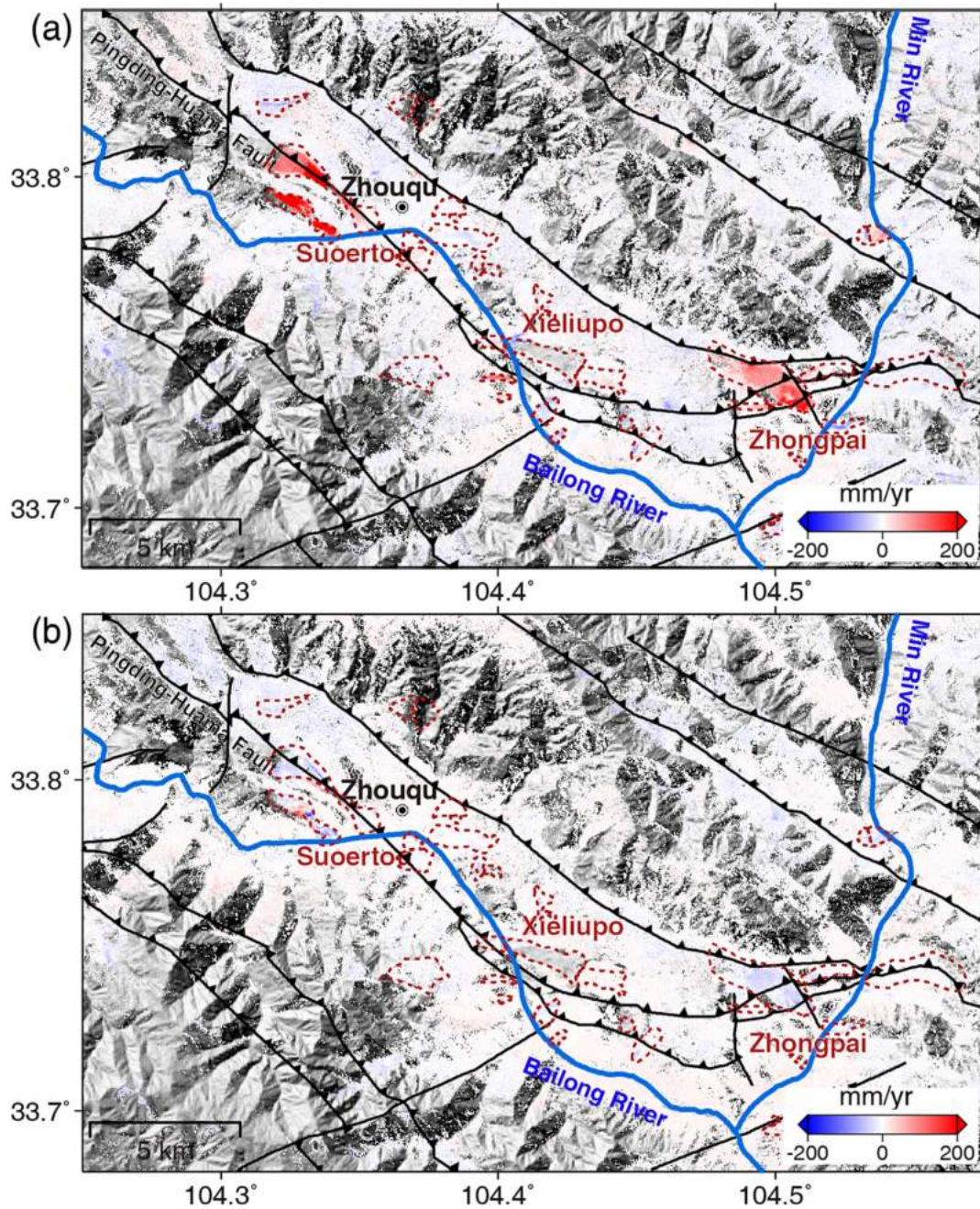
FIGURE 3 Displacement rates of Zhouqu County in the (a) eastward and (b) vertical directions. [Color figure can be viewed at wileyonlinelibrary.com]

at P1 and P2 were 2 and 5 mm and the standard deviations were 21 and 22 mm, respectively. The cumulative displacements in the downslope direction of P1 and P2 were 2 548 and 1 201 mm, respectively. The displacement at P1 and P2 accelerated during rainy seasons, especially during the water years of 2017–2019. The seasonal rainfall can elevate the pore water pressure at the base and thus decrease the shear strength (Hu et al., 2020).

The magnitude of eastward rate (460 mm/year) was about four times of than that in the vertical direction (−110 mm) (Figure 4c,d). The resolved accumulative eastward and vertical displacements were 1 618 and −217 mm at P1 and 487 and −64 mm at P2 from February 2017 to July 2020 in Figure 5b. The inferred eastward and vertical displacements at P1 and P2 exhibited seasonal variations. Figure 6 shows the eastward and vertical displacement rates of profile AA′, BB′ and CC′ crossing the Pingding-Huama fault. The displacement rates of

profile CC′ off the Suoertou landslide were generally less than ±10 mm/year.

The Daxiaowan landslide is approximately 2 800 m in length with an elevation difference of 850 m. The main sliding direction is S149°E with an average slope of 18° (Li et al., 2021). The Daxiaowan landslide has highly varied topography (Figure S3) and distinct materials (Li et al., 2021). The maximum LOS displacements of the landslide were −260 and 277 mm/year during 2015–2020 in the LOS direction from the S1-A and S1-D tracks, respectively (Figure 4a,b). Outstanding rates occurred at two blocks in the middle section and one block in the lower section (−113 to −13 mm/year), corresponding to three secondary landslides. The eastward rates were as large as 422 mm/year while the vertical rates varied between −185 and 154 mm/year. The cumulative downhill displacements of P3 and P4 (Figure 5c) reached 2 514 and 1 706 mm during 6 years, in phase with seasonal
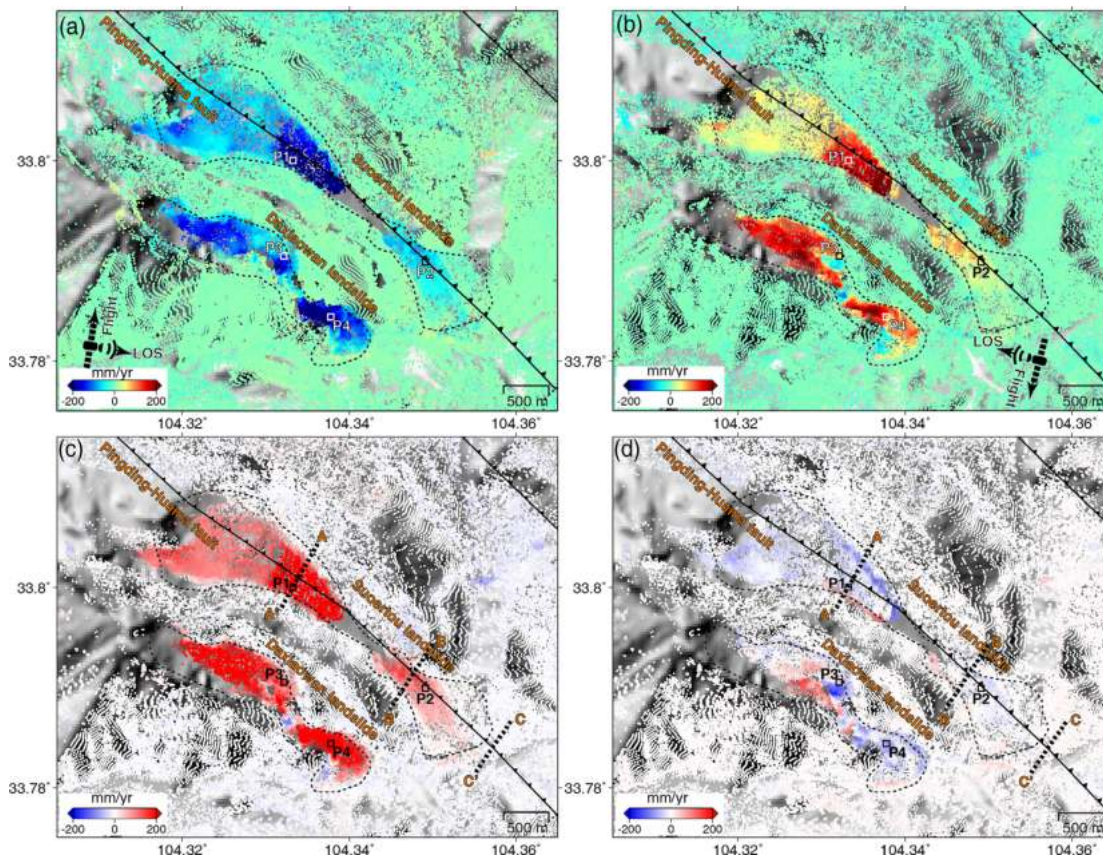
FIGURE 4 Displacement rates from (a) S1-A and (b) S1-D in the line-of-sight (LOS) and (c) eastward and (d) vertical directions of the Suoertou and Daxiaowan landslides. [Color figure can be viewed at wileyonlinelibrary.com]
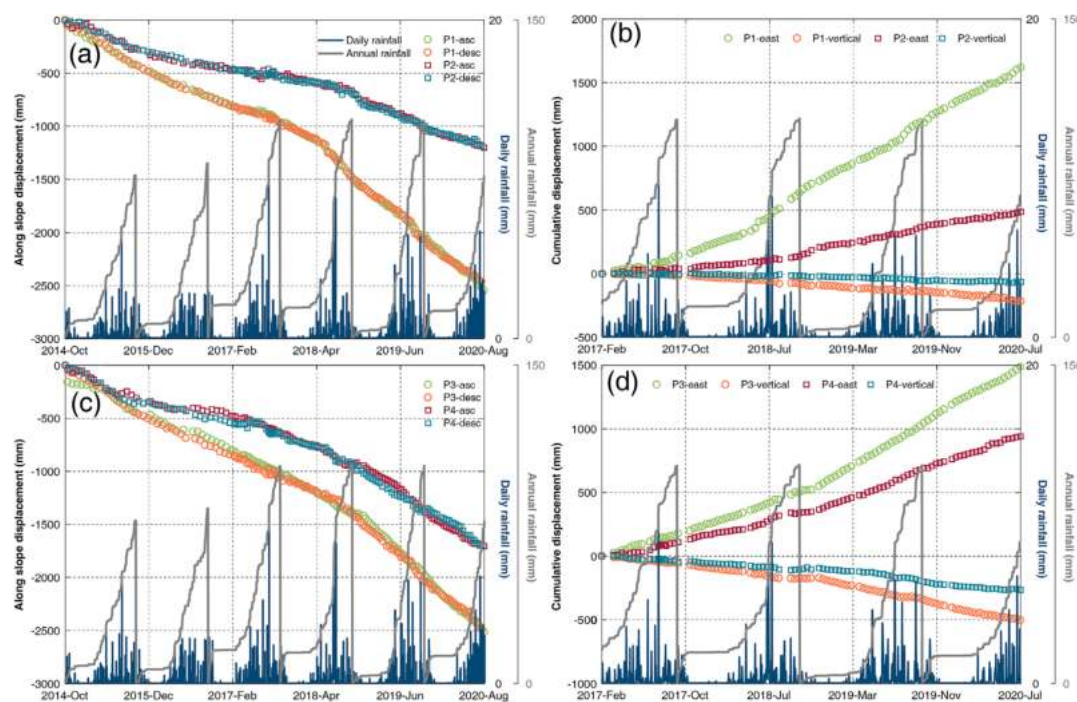

FIGURE 5 Cumulative slope-parallel displacements of (a) P1 and P2 on the Suoertou landslide and (c) P3 and P4 on the Daxiaowan landslide. Two-dimensional cumulative displacements of (b) P1 and P2 and (d) P3 and P4. [Color figure can be viewed at wileyonlinelibrary.com]

displacement variations of the Suoertou landslide. The average differences in downhill motions between the ascending and descending results were 18 and 11 mm on average at P3 and P4, and the standard deviations were 36 and 46 mm, respectively. The cumulative eastward

and vertical displacements from February 2017 to July 2020 were 1 487 and −504 mm at P3 and 941 and −266 mm at P4, respectively (Figure 5d). In addition, the displacement acceleration in 2018 related to the continuous rainfall. The eastward displacement rates increased

from 302 to 551 mm/year at P3 and from 210 to 345 mm/year at P4. The vertical displacement rates increased from −116 to −189 mm/year at P3 and from −64 to 104 mm/year at P4.

4.3 | Xieliupo landslide displacements

The Xieluiupo landslide is a tongue-shape debris slide with a length of ∼2 600 m and a width of ∼600 m (Figure 7). The sliding direction of the Xieliupo landslide is about N60°W with an average slope angle of 11° (Figure S4). It bounds the Pingding-Huama fault fractures. The landslide has been recognized as active with extensive fractures since 1963 (Dai et al., 2021), and eight rapid failures since 1904 (Jiang et al., 2016). The landslide has been moving slowly with displacement rates from sub-metre to several meters per year since the most recent failure in 1981 (Huang et al., 2013a; Jiang et al., 2016). Figure 7a,b show the LOS displacements from S1-A and S1-D tracks, respectively.

The displacement gradients in most of the Xieliupo landslide exceed the resolvability of InSAR using Sentinel-1 Interferometric Wide (IW) swath mode images (∼1 mm/day) (Li et al., 2023; Manconi, 2021). Therefore, valid pixels were only located over the less deforming foot of the Xieliupo landslide. The fastest displacement rates were −122 mm/year from S1-A track and 145 mm/year from S1-D track on slopes close to the Bailong River. The maximum horizontal rate was −214 mm/year westward while the vertical rates ranged from −62 to 84 mm/year (Figure 7c,d). The movements in the unmapped area (missing valid pixels in the middle of the transport zone) of the Xieliupo landslide were expected to be even faster. The upward displacement mainly concentrated at the southern distal area which might be caused by the compression and material accumulation. The along slope displacements at P5 reached −851 mm from 2014 to 2020 with an overall linear displacement trend (Figure 8). The average difference between the common-day downhill movements inferred from S1-A and S1-D tracks was 2 mm. The westward
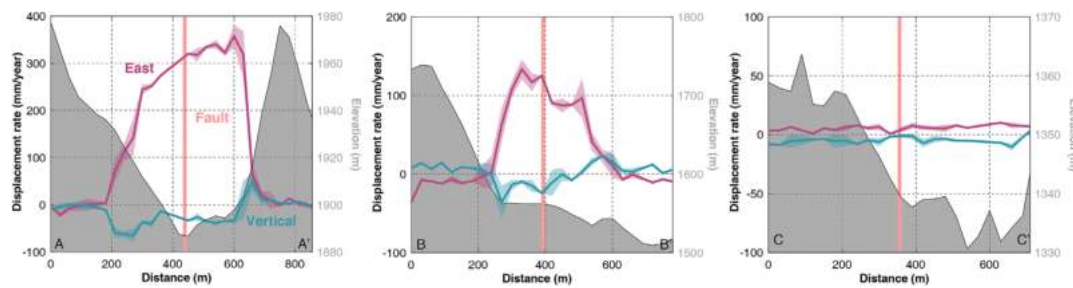

FIGURE 6 Cross-sections AA′ (on-slide), BB′ (on-slide) and CC′ (off-slide) of Suoertou landslide. Location of profiles are marked in Figure 4. [Color figure can be viewed at wileyonlinelibrary.com]
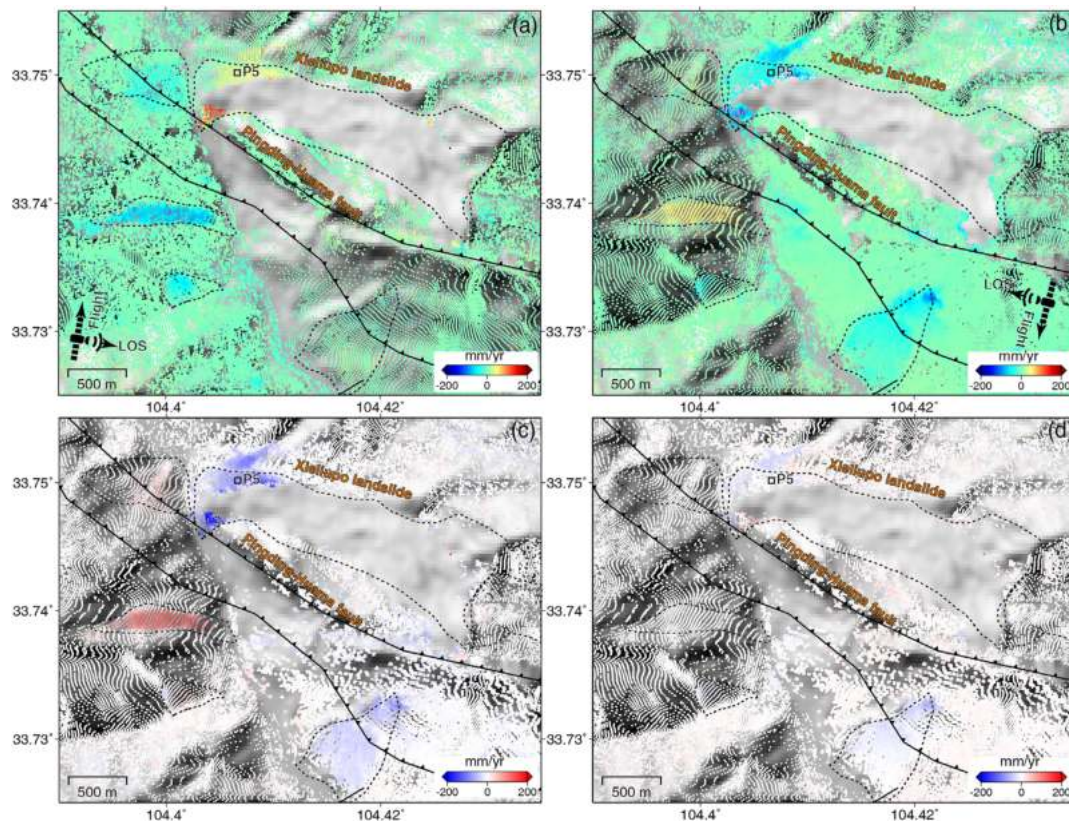

FIGURE 7 Displacement rates from (a) S1-A and (b) S1-D in the line-of-sight (LOS) and (c) eastward and (d) vertical directions of the Xieliupo landslide. [Color figure can be viewed at wileyonlinelibrary.com]
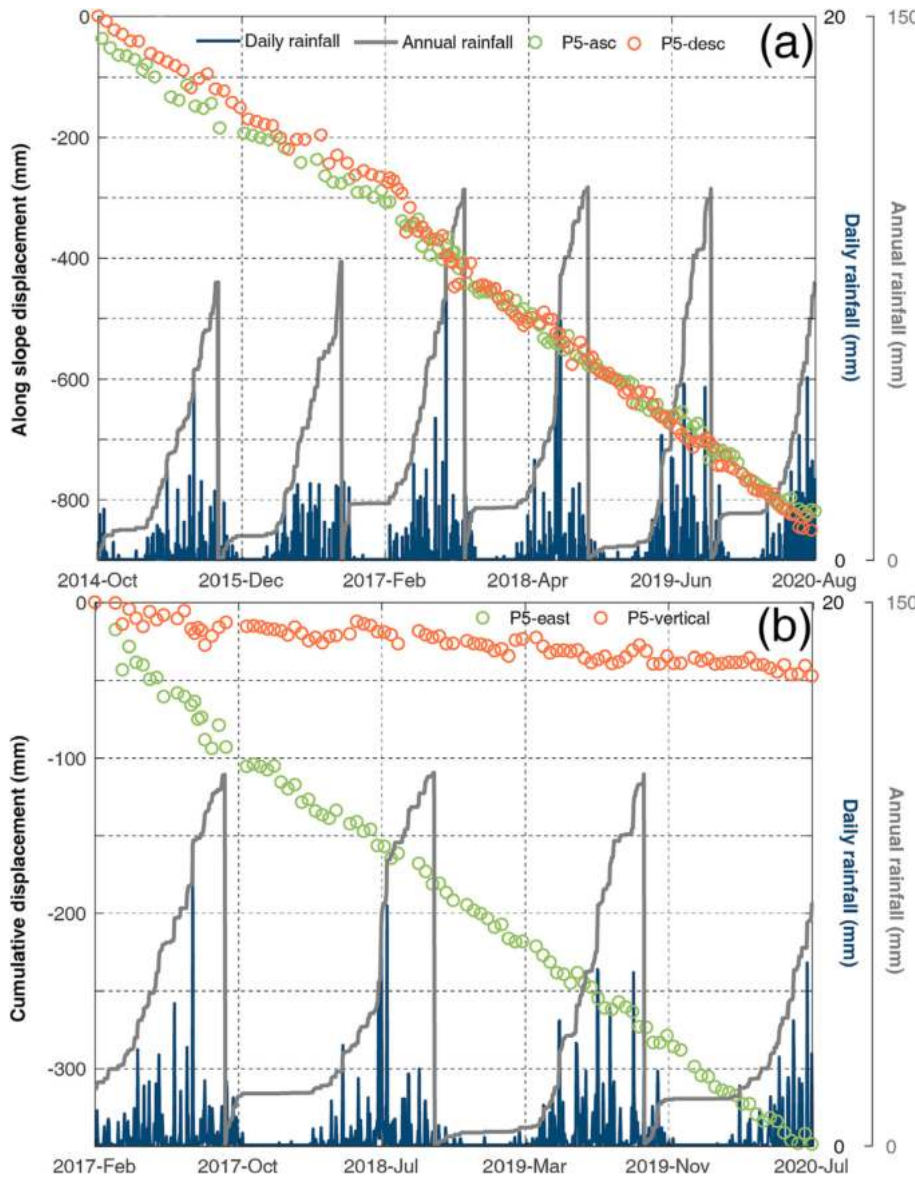
FIGURE 8 (a) Cumulative slope-parallel displacements and (b) two-dimensional displacements of P5 on the Xieliupo landslide. [Color figure can be viewed at wileyonlinelibrary.com]

accumulative displacements (349 mm) were much larger than the vertical accumulative displacements (−47 mm) from February 2017 to July 2020. The decomposed 2D displacement time series illuminate the kinematics of Xieliupo landslide better than InSAR LOS measurements. We note apparent rainfall-correlated seasonal variations in the vertical displacement component rather than westward displacement component.

4.4 | Zhongpai landslide displacements

The Zhongpai landslide in the intersection area of multiple faults is a giant mobile mass (>9.9 × 10⁷ m³) (Yang et al., 2013). The length and width of the landslide are approximately 3 500 and 1 000 m, respectively. The landslide is nested in the residential areas and cultivated lands (Figure S5). Figure 9 shows the LOS displacements from S1-A and S1-D tracks and the inferred 2D displacement maps of the Zhongpai landslide. The maximum rates were −156 and 159 mm/year in the LOS direction from S1-A and S1-D tracks, respectively. The maximum horizontal rate to the east (248 mm/yr) was much larger than that in the vertical direction (−87 mm/year). The displacement

rates decreased from the lower part where the faults cutting through the upper part of the landslide. The highly fractured rock along the fault zone facilitated landslide movements. Moderate upward movements at 20–60 mm/year occurred at the foot of the Zhongpai landslide with slopes less than 10° (Figure S6). Our results of the 2D decomposed displacements are primarily eastward and downward. Maximum eastward rates are more than three times of the maximum subsidence rates (Figure S7).

The off-slide, cross-fault profile FF′ has shown insignificant difference in displacement rates. On the other hand, the on-slide, cross-fault profile DD′ presented distinct rate differences in both eastward and vertical directions at the intersection with fault segments F1 and F2 (locations marked in Figure 9) while the variations crossing the PH fault was still minor (Figure 10). The faults cutting through the Zhongpai landslide might regulate the active margins and displacement distributions of the landslide system.

P6 in the lower section and P7 in the middle section of the Zhongpai landslide were selected for the time series analysis. The cumulative slope-parallel displacements of P6 and P7 were −1 330 and −846 mm from October 2014 to August 2020 (Figure 11). The average differences of the common-day measurement of S1-A
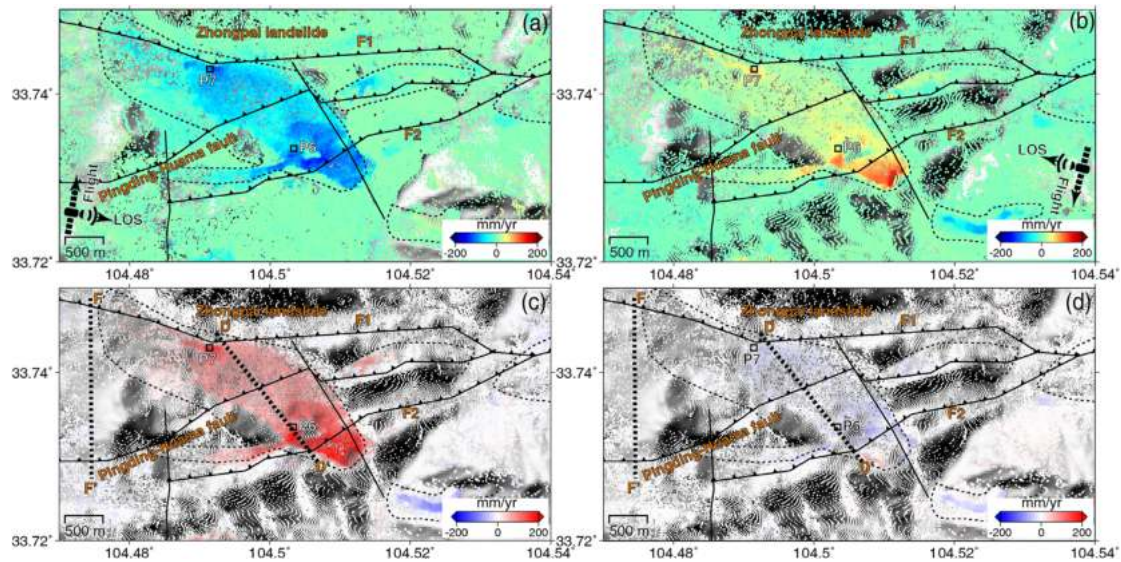
FIGURE 9 Displacement rates from (a) S1-A and (b) S1-D in the line-of-sight (LOS) and (c) eastward and (d) vertical directions of the Zhongpai landslide. The displacement rates of cross sections DD′ and FF′ are given in Figure 10. [Color figure can be viewed at wileyonlinelibrary.com]
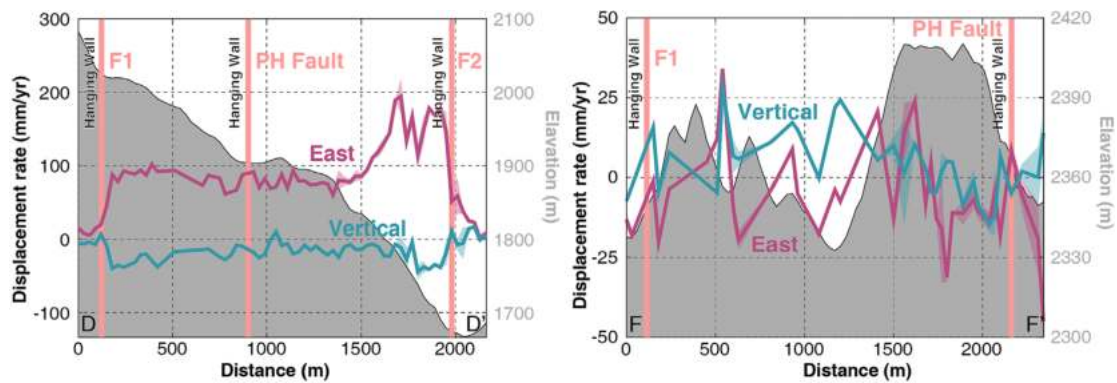

FIGURE 10 2D displacement rate cross-sections DD′ and FF′ of Zhongpai landslide. The locations for profiles and fault segments (F1 and F2) are marked in Figure 9. [Color figure can be viewed at wileyonlinelibrary.com]

and S1-D tracks were 4 mm at P6 and 2 mm at P7, respectively. The cumulative eastward and vertical displacements were 460 and −36 mm at P6 and 329 and −44 mm between February 2017 and July 2020, respectively. Seasonal accelerations correlated with the rainfall, especially pronounced during 2018 and 2019.

5 | DISCUSSION

Landslide movements in Zhouqu are controlled by multiple factors, for example, faults, lithology, rainfall, irrigation and other anthropogenic activities (Jiang & Wen, 2014; Yu et al., 2015; Zhang et al., 2012b; Zhang et al., 2018).

Tectonic movements and dynamic earthquakes create fractures on the landslide surfaces. The E-W strike of the Pingding-Huama fault controls the moving directions of massive landslides, for example, the Suoertou and Zhongpai landslides (Figures 6 and 10). Secondary landslides with surface fractures formed within giant landslides, for example, Suoertou, Daxiaowan, Xieliupo and Zhongpai landslides (Figures 4, 7 and 9). The displacement rates are different among

kinematic structures within a landslide. The persistent crustal uplift has steepened the slopes since the Quaternary, producing a large topographic relief (Huang et al., 2013a). The reported slip rates of Pingding-Huama fault were less than 4 mm/year (Chen et al., 2012; Yu et al., 2012). It is challenging to resolve this signal in vegetated hillslopes using InSAR method. Tectonic movements aggravate the rock and soil fragmentation. Co-seismic water level changes suggest that earthquakes may change the permeability of the rock mass, which may further entrap groundwater in the critical shear zone. In the meantime, several devastating earthquakes near Zhouqu led to fault zone weakening, rock shattering, slope titling and topographic amplification (Cui et al., 2013). Earth shaking displaces the mass, creates cracks and loose materials at the surface (Hu et al., 2018a), reduces the mechanical strength of rock and soil mass and may break the stress equilibrium of the slopes.

Other natural triggers, such as rainfall and river erosion, may jointly lead to accelerations and rapid failures of landslide systems. Rainwater can penetrate through the fractures and increase the pore water pressure at the critical shear zone (Hu et al., 2021). The seasonal accelerations or even dynamic failures usually occur during wet
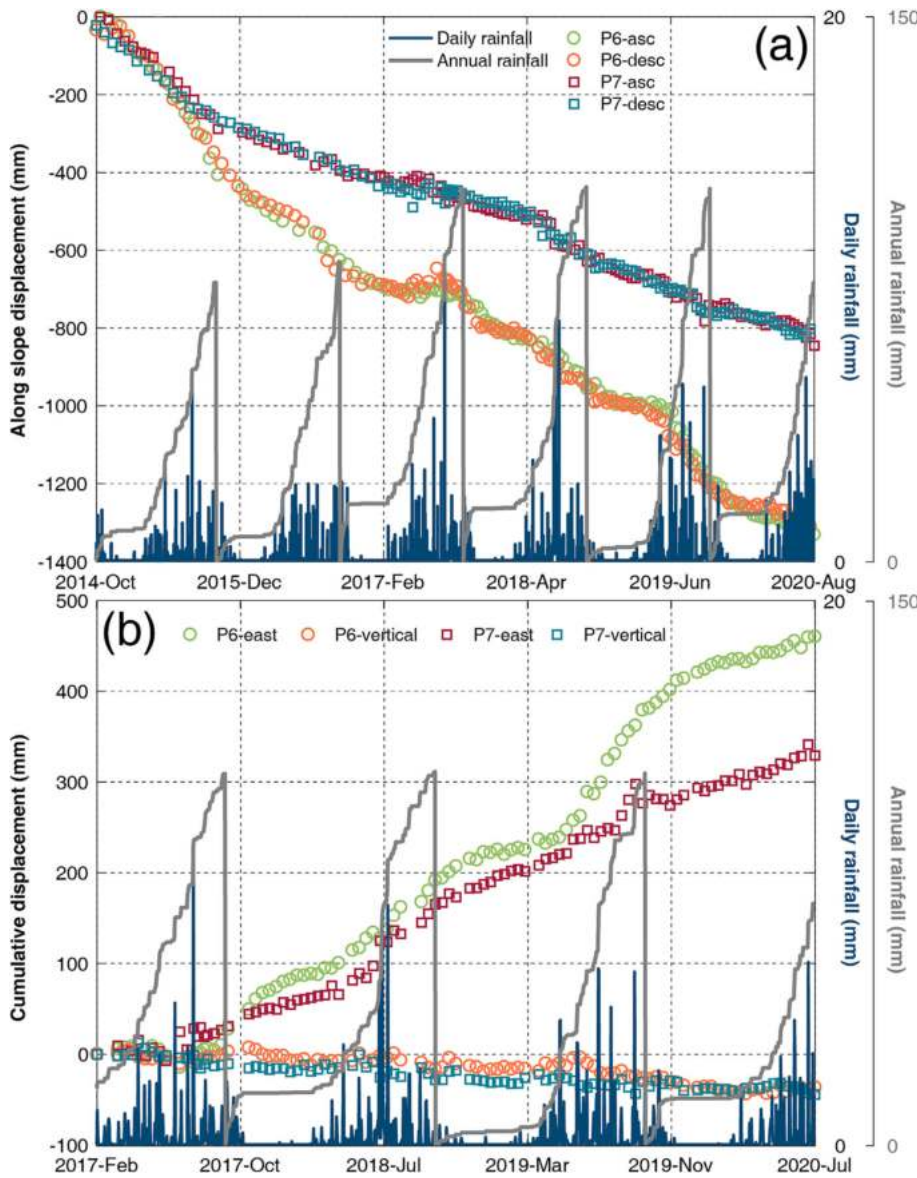
FIGURE 11 (a) Cumulative slope displacement-parallel displacements, and (b) two-dimensional displacements of P5 on Xieliupo landslide. [Color figure can be viewed at wileyonlinelibrary.com]

seasons. Rainstorm usually triggered landslides in Zhouqu (Ren et al., 2011). For example, the Jiangdingya and Yahuokou landslides and Sanyanyu debris flows (Figure 1) all occurred during the monsoonal summertime with abundant rainfall. Guo et al. (2019) reported that the daily precipitation on 25 June, 28 June, 29 June and 10 July 2018 reached 33, 48, 48 and 65 mm, respectively. The heavy rainfall not only triggered the collapse of the Jiangdingya landslide in 2018 but also accelerated the displacements of other landslides such as Suoertou and Daxiaowan landslides (Figure 5). Long-term (decadal) displacement monitoring can be helpful to determine the rainfall thresholds for landslide instability. The landslide toe erosion by the Bailong River further destabilizes the slopes due to the wear and tear of the landslide toe by the river water (Zhang et al., 2016). Nonetheless, the simulation results at the Suoertou landslide (Jiang et al., 2015) suggest that the river erosion only plays a minor role and the seismic shaking and groundwater variations have a greater impact on the slope stability.

Anthropogenic activities also affect landslide behaviors. Deforestation makes the slopes in Zhouqu region vulnerable to landsliding (Ren, 2014). Our detected landslides are located on or close to man-made structures and farmland (Figure S1). The man-made structures were mainly built on a relatively flat or low-lying areas which might affect the surface water runoff and groundwater flows as well as the vegetation growth. The construction of the S313 highway at the toe of Xieliupo landslide (Huang et al., 2013a; Jiang et al., 2016) and Daxiaowan landslide (Li et al., 2021) caused small-scale failures; similar phenomena were observed in the Monroe landslide in northern California, USA (Hu et al., 2019). Human activities including cultivation in the Daxiaowan and Zhongpai landslides might facilitate the formation and development of scrapes and cracks (Figure S5). Agricultural irrigations on landslide-prone region may lead to localized pore water pressure increase and the shear strength reduction (Shi et al., 2019a), as documented in Palu Valley in Indonesia where landslides, aqueducts and faults coexist (Bradley et al., 2019).

6 | CONCLUDING REMARKS

We mapped the landslide displacements in Zhouqu during 2014 and 2020 using the ascending and descending Sentinel-1 satellite images. Time-dependent 2D displacements between 2017 and 2020 were

extracted from ascending and descending scenes acquired on the same dates. Our detected landslides are nested in the active Pingding-Huama fault zone with well-developed factures. Displacement rates showed large variations in Suoertou and Zhongpai landslides. The eastward displacement rates were three to four times of that in the vertical direction. Abrupt displacement variations were overlapped with some Pingding-Huama fault segments in Suoertou and Zhongpai landslides. Displacement velocities obtained from satellite interferometry shows that faults control the distribution of landslide displacements and sometimes also define the boundaries of landslide systems. Seasonal rainfall is correlated with displacement time series, and the seasonal amplitude of displacement is proportional to the rainfall intensity. SAR satellite images can provide explicit spatiotemporal displacement details over landslides and is an important complement to *in situ* surveying tools in harsh natural environments.

CONFLICT OF INTEREST STATEMENT

We declare no conflict of interest. We grant the permission to reproduce material from other sources.

DATA AVAILABILITY STATEMENT

The Copernicus Sentinel-1 data were provided by European Space Agency (ESA) through the Alaska Satellite Facility (ASF).

ORCID

Xuguo Shi https://orcid.org/0000-0003-2815-7897

Xie Hu https://orcid.org/0000-0002-6744-7291

REFERENCES

Bai, S., Wang, J., Zhang, Z. & Cheng, C. (2012) Combined landslide susceptibility mapping after Wenchuan earthquake at the Zhouqu segment in the Bailongjiang Basin, China. *Catena*, 99, 18–25. Available from: https://doi.org/10.1016/j.catena.2012.06.012

Berardino, P., Fornaro, G., Lanari, R. & Sansosti, E. (2002) A new algorithm for surface deformation monitoring based on small baseline differential SAR interferograms. *IEEE Transactions on Geoscience and Remote Sensing*, 40(11), 2375–2383. Available from: https://doi.org/10.1109/TGRS.2002.803792

Bontemps, N., Lacroix, P., Larose, E., Jara, J. & Taipe, E. (2020) Rain and small earthquakes maintain a slow-moving landslide in a persistent critical state. *Nature Communications*, 11(1), 780. Available from: https://doi.org/10.1038/s41467-020-14445-3

Bradley, K., Mallick, R., Andikagumi, H., Hubbard, J., Meilianda, E., Switzer, A., et al. (2019) Earthquake-triggered 2018 Palu Valley landslides enabled by wet rice cultivation. *Nature Geoscience*, 12(11), 935–939. Available from: https://doi.org/10.1038/s41561-019-0444-1

Brown, C.F., Brumby, S.P., Guzder-Williams, B., Birch, T., Hyde, S.B., Mazzariello, J., et al. (2022) Dynamic world, near real-time global 10 m land use land cover mapping. *Scientific Data*, 9(1), 251. Available from: https://doi.org/10.1038/s41597-022-01307-4

Cheaib, A., Lacroix, P., Zerathe, S., Jongmans, D., Ajorlou, N., Doin, M.-P., et al. (2022) Landslides induced by the 2017 Mw7.3 Sarpol Zahab earthquake (Iran). *Landslides*, 19(3), 603–619. Available from: https://doi.org/10.1007/s10346-021-01832-0

Chen, C., Ren, J., Meng, G., Yang, P., Zhang, J. & Su, X. (2012) Analysis of modern activity of major faults in northeast margin of Baryan-Har block. *Journal of Geodesy and Geodynamics*, 32, 27–30.

Chen, Q., Cheng, H., Yang, Y., Liu, G. & Liu, L. (2014) Quantification of mass wasting volume associated with the giant landslide Daguangbao induced by the 2008 Wenchuan earthquake from persistent scatterer InSAR. *Remote Sensing of Environment*, 152, 125–135. Available from: https://doi.org/10.1016/j.rse.2014.06.002

Cui, P., Zhou, G.G.D., Zhu, X.H. & Zhang, J.Q. (2013) Scale amplification of natural debris flows caused by cascading landslide dam failures. *Geomorphology*, 182, 173–189. Available from: https://doi.org/10.1016/j.geomorph.2012.11.009

Dai, C., Li, W., Wang, D., Lu, H., Xu, Q. & Jian, J. (2021) Active landslide detection based on Sentinel-1 data and InSAR Technology in Zhouqu County, Gansu Province, Northwest China. *Journal of Earth Science*, 32(5), 1092–1103. Available from: https://doi.org/10.1007/s12583-020-1380-0

Dou, X. & Zhang, Z. (2021) Mechanism and causal analysis on the Yahuokou landslide reactivation and causes (Zhouqu County, Gansu, China). *The Chinese Journal of Geological Hazard and Control*, 32, 9–18.

Fan, M. (2006) *The analysis of forming rainstorm and Reseacrh about causing mud-rock flow and landslide in Longnan*. Nanjing: Nanjing University of Information Science and Technology.

Fan, X., Scaringi, G., Korup, O., West, A.J., van Westen, C.J., Tanyas, H., et al. (2019) Earthquake-induced chains of geologic hazards: Patterns, mechanisms, and impacts. *Reviews of Geophysics*, 57(2), 421–503. Available from: https://doi.org/10.1029/2018RG000626

Fan, X., Yunus, A.P., Scaringi, G., Catani, F., Siva Subramanian, S., Xu, Q., et al. (2021) Rapidly evolving controls of landslides after a strong earthquake and implications for Hazard assessments. *Geophysical Research Letters*, 48, e2020GL090509.

Ferretti, A., Prati, C. & Rocca, F. (2001) Permanent scatterers in SAR interferometry. *IEEE Transactions on Geoscience and Remote Sensing*, 39(1), 8–20. Available from: https://doi.org/10.1109/36.898661

Froude, M.J. & Petley, D.N. (2018) Global fatal landslide occurrence from 2004 to 2016. *Natural Hazards and Earth System Sciences*, 18(8), 2161–2181. Available from: https://doi.org/10.5194/nhess-18-2161-2018

Fujiwara, S., Nishimura, T., Murakami, M., Nakagawa, H., Tobita, M. & Rosen, P.A. (2000) 2.5-D surface deformation of M6.1 earthquake near Mt Iwate detected by SAR interferometry. *Geophysical Research Letters*, 27(14), 2049–2052. Available from: https://doi.org/10.1029/1999GL011291

Goldstein, R.M. & Werner, C.L. (1998) Radar interferogram filtering for geophysical applications. *Geophysical Research Letters*, 25(21), 4035–4038. Available from: https://doi.org/10.1029/1998GL900033

Guo, C., Ren, S., Li, X., Zhang, Y., Yang, Z., Wu, R., et al. (2019) Development characteristics and reactivation mechanism of the Jiangdingya ancient landslide in the Nanyu town, Zhouqu County, Gansu Province. *Geoscience*, 33, 206–217.

Hanssen, R.F. (2001) *Radar interferometry: Data interpretation and error analysis*. Dordrecht: Springer. https://doi.org/10.1007/0-306-47633-9

Hou, S., Li, A., Chen, L., Feng, Z., Wang, L., Cao, P., et al. (2020) Application of universal geo-hazard monitoring instruments in landslides and early warning of three landslides in Gansu Province: A case study in Minxian County and Lanzhou City of Gansu Province. *The Chinese Journal of Geological Hazard and Control*, 31, 47–53.

Hu, J., Li, Z.W., Ding, X.L., Zhu, J.J., Zhang, L. & Sun, Q. (2014) Resolving three-dimensional surface displacements from InSAR measurements: A review. *Earth-Science Reviews*, 133, 1–17. Available from: https://doi.org/10.1016/j.earscirev.2014.02.005

Hu, K., Ge, Y. & Cui, P. (2010) Preliminary analysis of extra-large-scale debris flow disaster in Zhouqu County of Gansu Province. *Journal of Mountain Science*, 28, 628–634.

Hu, W., Li, Y., Gou, H., Van Asch, T.W.J., Gao, X., Zheng, Y., et al. (2021) Hydraulic properties of co-seismic landslide deposits around the Wenchuan earthquake epicentre: Large-scale column experiments.

Engineering Geology, 287, 106102. Available from: https://doi.org/10.1016/j.enggeo.2021.106102

Hu, W., Scaringi, G., Xu, Q. & Huang, R. (2018a) Internal erosion controls failure and runout of loose granular deposits: Evidence from flume tests and implications for Postseismic slope healing. *Geophysical Research Letters*, 45(11), 5518–5527. Available from: https://doi.org/10.1029/2018GL078030

Hu, X., Bürgmann, R., Lu, Z., Handwerger, A.L., Wang, T. & Miao, R. (2019) Mobility, thickness, and hydraulic diffusivity of the slow-moving Monroe landslide in California revealed by L-band satellite radar interferometry. *Journal of Geophysical Research: Solid Earth*, 124(7), 7504–7518. Available from: https://doi.org/10.1029/2019JB017560

Hu, X., Bürgmann, R., Schulz, W.H. & Fielding, E.J. (2020) Four-dimensional surface motions of the Slumgullion landslide and quantification of hydrometeorological forcing. *Nature Communications*, 11(1), 2792. Available from: https://doi.org/10.1038/s41467-020-16617-7

Hu, X., Lu, Z., Pierson, T.C., Kramer, R. & George, D.L. (2018b) Combining InSAR and GPS to determine transient movement and thickness of a seasonally active low-gradient translational landslide. *Geophysical Research Letters*, 45(3), 1453–1462. Available from: https://doi.org/10.1002/2017GL076623

Huang, R. & Li, W. (2011) Formation, distribution and risk control of landslides in China. *Journal of Rock Mechanics and Geotechnical Engineering*, 3(2), 97–116. Available from: https://doi.org/10.3724/SP.J.1235.2011.00097

Huang, X., Yang, W., Zhang, C., Shen, J. & Liu, T. (2013a) Deformation characteristics and formation mechanism of Xieliupo landslide in Zhouqu. *Journal of Geomechanics*, 19, 178–187.

Huang, X., Yang, W., Zhang, C., Shen, J. & Liu, T. (2013b) The formation mechanism of Suoertou landslide in Pingding-Huama fault zone, southern Gansu. *Geological Bulletin of China*, 32, 1936–1942.

Jiang, M. (2020) Sentinel-1 TOPS co-registration over low-coherence areas and its application to velocity estimation using the all pairs shortest path algorithm. *Journal of Geodesy*, 94(10), 95. Available from: https://doi.org/10.1007/s00190-020-01432-1

Jiang, S., Wen, B.-P., Zhao, C., Li, R.-D. & Li, Z.-H. (2016) Kinematics of a giant slow-moving landslide in Northwest China: Constraints from high resolution remote sensing imagery and GPS monitoring. *Journal of Asian Earth Sciences*, 123, 34–46. Available from: https://doi.org/10.1016/j.jseaes.2016.03.019

Jiang, X. & Wen, B. (2014) Creep Behavior of the Slip Zone of a Giant Slow-Moving Landslide in Northwest China: The Suoertou Landslide as an Example. In: Sassa, K., Canuti, P. & Yin, Y. (Eds.) *Landslide science for a safer Geoenvironment*. Cham: Springer International Publishing, pp. 141–145 https://doi.org/10.1007/978-3-319-05050-8_23

Jiang, X., Wen, B., Jiang, S., Feng, C., Zhao, C. & Li, R. (2015) Main factors analysis for controlling kinematic behavior of Suoertou landslide. *Journal of Jilin University (Earth Science Edition)*, 45, 1798–1807.

Kirby, E., Whipple, K.X., Tang, W. & Chen, Z. (2003) Distribution of active rock uplift along the eastern margin of the Tibetan plateau: Inferences from bedrock channel longitudinal profiles. *Journal of Geophysical Research: Solid Earth*, 108(B4), ETG16-1. Available from: https://doi.org/10.1029/2001JB000861

Lacroix, P., Dehecq, A. & Taipe, E. (2020) Irrigation-triggered landslides in a Peruvian desert caused by modern intensive farming. *Nature Geoscience*, 13(1), 56–60. Available from: https://doi.org/10.1038/s41561-019-0500-x

Lacroix, P., Perfettini, H., Taipe, E. & Guillier, B. (2014) Coseismic and postseismic motion of a landslide: Observations, modeling, and analogy with tectonic faults. *Geophysical Research Letters*, 41(19), 6676–6680. Available from: https://doi.org/10.1002/2014GL061170

Li, M., Zhang, L., Yang, M. & Liao, M. (2023) Complex surface displacements of the Nanyu landslide in Zhouqu, China revealed by multi-platform InSAR observations. *Engineering Geology*, 317, 107069. Available from: https://doi.org/10.1016/j.enggeo.2023.107069

Li, Y., Zhang, Y., Meng, X., Chen, G., Zeng, R., Yue, D., et al. (2021) Analysis the activity characteristics of the giant landslide in active tectonic

fault zone: A case study of Daxiaowan landslide in Bailong River basin. *Journal of Lanzhou University (Natural Sciences)*, 57, 360–368.

Lu, Z. & Dzurisin, D. (2014) *InSAR imaging of Aleutian volcanoes: Monitoring a volcanic arc from space*. Berlin: Springer.

Ma, S., Qiu, H., Hu, S., Yang, D. & Liu, Z. (2021) Characteristics and geomorphology change detection analysis of the Jiangdingya landslide on July 12, 2018, China. *Landslides*, 18(1), 383–396. Available from: https://doi.org/10.1007/s10346-020-01530-3

Manconi, A. (2021) How phase aliasing limits systematic space-borne DInSAR monitoring and failure forecast of alpine landslides. *Engineering Geology*, 287, 106094. Available from: https://doi.org/10.1016/j.enggeo.2021.106094

Meng, X., Chen, G., Guo, P., Xiong, M. & Janusz, W. (2013) Research of landslides and debris flows in Bailong River basin: Progress and prospect. *Marine Geology & Quaternary Geology*, 033(4), 1–15. Available from: https://doi.org/10.3724/SP.J.1140.2013.04001

Qi, T., Meng, X., Qing, F., Zhao, Y., Shi, W., Chen, G., et al. (2021) Distribution and characteristics of large landslides in a fault zone: A case study of the NE Qinghai-Tibet plateau. *Geomorphology*, 379, 107592. Available from: https://doi.org/10.1016/j.geomorph.2021.107592

Ren, D. (2014) The devastating Zhouqu storm-triggered debris flow of august 2010: Likely causes and possible trends in a future warming climate. *Journal of Geophysical Research: Atmospheres*, 119(7), 3643–3662. Available from: https://doi.org/10.1002/2013JD020881

Ren, D., Fu, R., Leslie, L.M. & Dickinson, R.E. (2011) Predicting Storm-triggered Landslides. *Bulletin of the American Meteorological Society*, 92(2), 129–139. Available from: https://doi.org/10.1175/2010BAMS3017.1

Schäbitz, M., Janssen, C., Wenk, H.R., Wirth, R., Schuck, B., Wetzel, H.U., et al. (2018) Microstructures in landslides in Northwest China – implications for creeping displacements? *Journal of Structural Geology*, 106, 70–85. Available from: https://doi.org/10.1016/j.jsg.2017.11.009

Schmidt, D.A. & Bürgmann, R. (2003) Time-dependent land uplift and subsidence in the Santa Clara valley, California, from a large interferometric synthetic aperture radar data set. *Journal of Geophysical Research*, 108, 2416.

Shi, X., Hu, X., Sitar, N., Kayen, R., Qi, S., Jiang, H., et al. (2021) Hydrological control shift from river level to rainfall in the reactivated Guobu slope besides the Laxiwa hydropower station in China. *Remote Sensing of Environment*, 265, 112664. Available from: https://doi.org/10.1016/j.rse.2021.112664

Shi, X., Wang, J., Jiang, M., Zhang, S., Wu, Y. & Zhong, Y. (2022) Extreme rainfall-related accelerations in landslides in Danba County, Sichuan Province, as detected by InSAR. *International Journal of Applied Earth Observation and Geoinformation*, 115, 103109. Available from: https://doi.org/10.1016/j.jag.2022.103109

Shi, X., Xu, Q., Zhang, L., Zhao, K., Dong, J., Jiang, H., et al. (2019a) Surface displacements of the Heifangtai terrace in Northwest China measured by X and C-band InSAR observations. *Engineering Geology*, 259, 105181. Available from: https://doi.org/10.1016/j.enggeo.2019.105181

Shi, X., Yang, C., Zhang, L., Jiang, H., Liao, M., Zhang, L., et al. (2019b) Mapping and characterizing displacements of active loess slopes along the upstream Yellow River with multi-temporal InSAR datasets. *Science of the Total Environment*, 674, 200–210. Available from: https://doi.org/10.1016/j.scitotenv.2019.04.140

Shu, X. & Yang, R. (2012) Deep causes and prevention of the catastrophic debris flow in Zhouqu County. *Bulletin of Soil and Water Conservation*, 32, 18–22.

Sun, Q., Hu, J., Zhang, L. & Ding, X. (2016) Towards slow-moving landslide monitoring by integrating multi-sensor InSAR time series datasets: The Zhouqu case study, China. *Remote Sensing*, 8(11), 908. Available from: https://doi.org/10.3390/rs8110908

Sun, Q., Zhang, L., Ding, X., Hu, J., Li, Z. & Zhu, J. (2015) Slope deformation prior to Zhouqu, China landslide from InSAR time series analysis. *Remote Sensing of Environment*, 156, 45–57. Available from: https://doi.org/10.1016/j.rse.2014.09.029

Tang, C., Rengers, N., Asch, T.V., Yang, Y.H. & Wang, G.F. (2011) Triggering conditions and depositional characteristics of a disastrous debris flow

event in Zhouqu city, Gansu Province, northwestern China. *Natural Hazards and Earth System Sciences*, 11(11), 2903–2912. Available from: https://doi.org/10.5194/nhess-11-2903-2011

Wang, G.L. (2013) Lessons learned from protective measures associated with the 2010 Zhouqu debris flow disaster in China. *Natural Hazards*, 69(3), 1835–1847. Available from: https://doi.org/10.1007/s11069-013-0772-1

Wasowski, J. & Bovenga, F. (2014) Investigating landslides and unstable slopes with satellite multi temporal interferometry: Current issues and future perspectives. *Engineering Geology*, 174, 103–138. Available from: https://doi.org/10.1016/j.enggeo.2014.03.003

Yang, W., Huang, X., Zhang, Y. & Liu, T. (2013) The deformation characteristics of the landslide along Pingding-Huama active fault zone and its prevention and control. *Geological Bulletin of China*, 32, 1925–1935.

Yu, G., Zhang, M., Cong, K. & Pei, L. (2015) Critical rainfall thresholds for debris flows in Sanyanyu, Zhouqu County, Gansu Province, China. *Quarterly Journal of Engineering Geology and Hydrogeology*, 48(3-4), 224–233. Available from: https://doi.org/10.1144/qjegh2014-078

Yu, J., Zheng, W., Yuan, D., Pang, J., Liu, X. & Liu, B. (2012) Late quaternary active characteristics and slip-rate of Pingding-Huama fault, the eastern segment of Guanggaishan-Dieshan fault zone (West Qinlin Mountain). *Quaternary Sciences*, 032, 957–967.

Zhang, L., Lu, Z., Ding, X., Jung, H.-S., Feng, G. & Lee, C.-W. (2012a) Mapping ground surface deformation using temporarily coherent point SAR interferometry: Application to Los Angeles Basin. *Remote Sensing of Environment*, 117, 429–439. Available from: https://doi.org/10.1016/j.rse.2011.10.020

Zhang, Y., Meng, X., Chen, G., Qiao, L., Zeng, R. & Chang, J. (2016) Detection of geohazards in the Bailong River basin using synthetic aperture radar interferometry. *Landslides*, 13(5), 1273–1284. Available from: https://doi.org/10.1007/s10346-015-0660-8

Zhang, Y., Meng, X., Jordan, C., Novellino, A., Dijkstra, T. & Chen, G. (2018) Investigating slow-moving landslides in the Zhouqu region of China using InSAR time series. *Landslides*, 15(7), 1299–1315. Available from: https://doi.org/10.1007/s10346-018-0954-8

Zhang, Z., Zhang, Q., Tao, J., Sun, Y. & Zhao, Q. (2012b) Climatic and geological environmental characteristics of the exceptional debris flow outburst in Zhouqu, Gansu Province, on 8 august, 2010. *Journal of Glaciology and Geocryology*, 34, 898–905.

SUPPORTING INFORMATION

Additional supporting information can be found online in the Supporting Information section at the end of this article.